# Supplementary Information: Fermi energy Weyl nodes in $AMTe_4$ (A=Ta, Nb, M=Ir, Rh)

Shivam Parasar[1], Jeroen van den Brink[2,3,*] & Rajyavardhan Ray[1,2,‡]

[1]*Department of Physics, Birla Institute of Technology Mesra, Ranchi, India - 835215*
[2]*Leibniz Institute for Solid-State and Materials Research (IFW) Dresden, Helmholtzstr. 20, 01069 Dresden, Germany*
[3]*Institute of Theoretical Physics and Würzburg-Dresden Cluster of Excellence ct.qmat, Technische Universität Dresden, 01062 Dresden, Germany*

## Suppementary Note I: Structural Details

The DFT calculations were carried out for $AM\text{Te}_4$ ($A$=Ta, Nb, $M$=Ir, Rh). For Ir-based $\text{TaIrTe}_4$ and $\text{NbIrTe}_4$, the reported experimental structures were used.[1,2] In addition, the atomic positions were optimized using local density approximation (LDA)[3] and generalized gradient approximation (GGA)[4] while keeping the lattice constants fixed to the experimental values. The force threshold of 0.001 ev/Åwas used. For $\text{TaRhTe}_4$, the reported structure[5] possesss a large residual forces, upto 0.07 eV/Å. As a result, only a structure with the same lattice parameters as the experimental structure, and optimized atomic positions were used. The lattice parameters of $\text{NbRhTe}_4$ were estimated by scaling the experimental lattice constants of $\text{NbIrTe}_4$ by the same ratios as that of the lattice constants of the experimental structures of $\text{TaIrTe}_4$ & $\text{TaRhTe}_4$. The atomic positions were relaxed while keeping the lattice constants fixed. The crystal structure details include lattice parameters, Wyckoff positions, corresponding atoms and their fractional coordinates $(x, y, z)$ and are listed in Tables S1, S2 & S3.

For $\text{TaIrTe}_4$ the largest deviation in atomic positions between experimental and LDA-optimized structure is observed to be 0.042 Å, and 0.046 Å between the LDA- and GGA-optimized structures. Whereas, for $\text{TaRhTe}_4$, the maximum shift between experimental and LDA-optimized structure is 0.388 Å. Between, LDA and GGA-optimized structures, only a difference of 0.046 Å was found.

## Suppementary Note II: Parameter Dependence

In Figs. S1 and S2, we show the sensititvity of the calculated bandstructures to various DFT parameters for $\text{TaIrTe}_4$ and $\text{TaRhTe}_4$. Using $\text{TaIrTe}_4$ we provide a detailed comparison of the electronic properties (bandstructure) between experimental and LDA-optimised crystal structures. Additionally we also show the effects of different $k$-mesh and XC functional in our study. For

$TaIrTe_4$, we also provide a comparison between different Wannier models — minimal basis vs full valence orbital basis. The minimal basis Wannier model was constructed by excluding the $(n+1)s$ orbital of Ir.

### Suppementary Note III: Quantum Oscillations (dHvA)

In Figs. S3, we show and compare the de Haas-van Alphen (dHvA) frequencies of $TaIrTe_4$ obtained from the experiments (Fig. S3 (a)),[6] with our calculations on experimental structure using a $k$-mesh with $120 \times 60 \times 60$ intervals along with LDA (Fig. S3 (b)) and GGA (Fig. S3 (c)) fuctionals. The curves $H_1$ corresponds to $F_3$, $H_2$ to $F_4$, $H_3$ to $F_2$, and $H_4$ to $F_1$. Since, the hole-pockets $H_2$ and $H_3$ along $\Gamma - X$ and $S - Y$, merges in our calculations, the dHvA frequencies shoots up along $B \parallel c$ direction. Interestingly, in the experimental structure the needle-like hole-pocket along $Y - \Gamma$ does not have an open Fermi surface, therefore, the corresponding dHvA frequency for $H_4$ does not shoot up and gives a finite value ($\sim 90$ T) along $B \parallel c$ direction.

In Fig. S3 (d), we also show the dHvA frequencies for the optimized crystal structure of $TaIrTe_4$ using a $k$-mesh with $120 \times 60 \times 60$ intervals and LDA fuctional. The behaviour of dHvA frequencies are similar to the results obtained through GGA on an optimized structure using a $k$-mesh with $20 \times 10 \times 10$ intervals. The curves $H_2$ and $H_3$ correspoding to hole-pockets along $\Gamma - X$ and $S - Y$, sees a sharp increase along $B \parallel c$ direction due to merging of pockets. The curve $H_4$ also shoots up, as the needle-like hole-pocket along $Y - \Gamma$ has an open Fermi surface in the optimized structures.

Further, as shown in Table S4, we evaluated the energies associated with these frequencies using the Onsager relation.[7] In Table S5, we present the energy shifts requried in the calculated hole pockets to have a good agreement with the experimental observations.

### Suppementary Note IV: Weyl Point Characteristics & Type

In Table S6, S7, S8 & S9, we provide a complete description of Weyl points (WPs) identified in $TaIrTe_4$, $TaRhTe_4$, $NbIrTe_4$ and $NbRhTe_4$. For each WP, we specify the band contributions, energy values, their chiralities, Brillouin zone positions, and their degeneracy.

Additionally, for selected WPs close to the Fermi energy ($|E_{WP}| < 50$ meV), we determine the WP-type. For this purpose, we study the dispersion along the principle directions. In other words, for a WP located at $(k_x, k_y, k_z)$, we obtained the WP dispersion in these three directions:

- Line passing through WP, $\parallel$ to $x$-axis : $(0, k_y, 0) \rightarrow (k_x, k_y, k_z) \rightarrow (1/2, k_y, 0)$
- Line passing through WP, $\parallel$ to $y$-axis : $(k_x, 0, 0) \rightarrow (k_x, k_y, k_z) \rightarrow (k_x, 1/2, 0)$

- Line passing through WP, $\parallel$ to $z$-axis : $(k_x, k_y, 1/4) \rightarrow (k_x, k_y, k_z) \rightarrow (1/2, k_y, -1/4)$

Figures S4 - S11 show the low-energy dispersion of these WPs. Note that in the figures, dispersions are shown only along a segment of the above lines.

## Suppementary Note V: Fermi Surface of Nb-Compounds

In Fig. S12, we show the calculated FS of Nb$M$Te$_4$ ($M$= Ir, Rh) using a $k$-mesh with $120 \times 60 \times 60$ intervals together with GGA functional. Similar to its Ta counterpart, NbIrTe$_4$ also has merging of hole-pockets $H_2$ and $H_3$. As a result of this merging, we observe a sharp increase in the dHvA frequencies of these pockets along $B \parallel c$ direction. Since the fish-and-toad structure is $\sim 25$ meV below the Fermi level, a needle-like dispersion is not observed here.

NbRhTe$_4$ shares similar features in the FS as TaRhTe$_4$, with the exception of few missing hole pockets. The small electron-pocket along $S - Y$ and the needle-like dispersion along $Y - \Gamma$ are absent here, because the bands responsible for these structures are away from the Fermi level in NbRhTe$_4$ and do not contribute to the FS.

Table S1: Structural details of $TaIrTe_4$. Fractional atomic coordinates $(x, y, z)$ in the experimental, LDA-optimized and GGA-optimized structures. The lattice constants are kept fixed: $a = 3.77$ Å, $b = 12.421$ Å, $c = 13.184$ Å.

| | | Experimental str. | | | LDA-Opt str. | | | GGA-Opt str. | | |
|---|---|---|---|---|---|---|---|---|---|---|
| **No.** | **Atom** | $x$ | $y$ | $z$ | $x$ | $y$ | $z$ | $x$ | $y$ | $z$ |
| 1 | Ta | 0 | 0.0540 | 0.0041 | 0 | 0.0545 | 0.0041 | 0 | 0.0548 | 0.0041 |
| 2 | Ta | 0 | 0.2697 | 0.4910 | 0 | 0.2713 | 0.4901 | 0 | 0.2707 | 0.4900 |
| 3 | Ir | 0 | 0.5355 | 0 | 0 | 0.5359 | 0.9989 | 0 | 0.5367 | 0.9991 |
| 4 | Ir | 0 | 0.7543 | 0.4916 | 0 | 0.7570 | 0.4903 | 0 | 0.7577 | 0.4896 |
| 5 | Te | 0 | 0.0648 | 0.3897 | 0 | 0.0662 | 0.3905 | 0 | 0.0658 | 0.3878 |
| 6 | Te | 0 | 0.1937 | 0.8527 | 0 | 0.1923 | 0.8500 | 0 | 0.1919 | 0.8465 |
| 7 | Te | 0 | 0.3458 | 0.0957 | 0 | 0.3443 | 0.0950 | 0 | 0.3445 | 0.0966 |
| 8 | Te | 0 | 0.4142 | 0.6391 | 0 | 0.4148 | 0.6392 | 0 | 0.4142 | 0.6423 |
| 9 | Te | 0 | 0.5642 | 0.3960 | 0 | 0.5652 | 0.3936 | 0 | 0.5652 | 0.3914 |
| 10 | Te | 0 | 0.6776 | 0.8469 | 0 | 0.6782 | 0.8447 | 0 | 0.6787 | 0.8420 |
| 11 | Te | 0 | 0.8492 | 0.1078 | 0 | 0.8487 | 0.1062 | 0 | 0.8493 | 0.1088 |
| 12 | Te | 0 | 0.8933 | 0.6484 | 0 | 0.8951 | 0.6495 | 0 | 0.8954 | 0.6522 |

Table S2: Structural details of $TaRhTe_4$. Fractional atomic coordinates $(x, y, z)$ in the experimental, LDA-optimized and GGA-optimized structures, with the lattice constants: $a = 3.757$ Å, $b = 12.548$ Å, $c = 13.166$ Å.

| | | Experimental str. | | | LDA-Opt str. | | | GGA-Opt str. | | |
|---|---|---|---|---|---|---|---|---|---|---|
| **No.** | **Atom** | $x$ | $y$ | $z$ | $x$ | $y$ | $z$ | $x$ | $y$ | $z$ |
| 1 | Ta | 0 | 0.0558 | 0.8080 | 0 | 0.0531 | 0.8080 | 0 | 0.0534 | 0.8080 |
| 2 | Ta | 0 | 0.2653 | 0.2910 | 0 | 0.2708 | 0.2950 | 0 | 0.2701 | 0.2951 |
| 3 | Rh | 0 | 0.5276 | 0.8020 | 0 | 0.5347 | 0.8033 | 0 | 0.5354 | 0.8036 |
| 4 | Rh | 0 | 0.7543 | 0.3310 | 0 | 0.7559 | 0.2950 | 0 | 0.7563 | 0.2944 |
| 5 | Te | 0 | 0.0595 | 0.1905 | 0 | 0.0675 | 0.1954 | 0 | 0.0671 | 0.1927 |
| 6 | Te | 0 | 0.1945 | 0.6260 | 0 | 0.1914 | 0.6555 | 0 | 0.1908 | 0.6520 |
| 7 | Te | 0 | 0.3448 | 0.9081 | 0 | 0.3452 | 0.8980 | 0 | 0.3457 | 0.9001 |
| 8 | Te | 0 | 0.4078 | 0.4448 | 0 | 0.4139 | 0.4431 | 0 | 0.4129 | 0.4466 |
| 9 | Te | 0 | 0.5727 | 0.1998 | 0 | 0.5666 | 0.1996 | 0 | 0.5665 | 0.1971 |
| 10 | Te | 0 | 0.6773 | 0.6576 | 0 | 0.6761 | 0.6502 | 0 | 0.6769 | 0.6475 |
| 11 | Te | 0 | 0.8504 | 0.9226 | 0 | 0.8492 | 0.9104 | 0 | 0.8499 | 0.9131 |
| 12 | Te | 0 | 0.9044 | 0.4675 | 0 | 0.8937 | 0.4525 | 0 | 0.8942 | 0.4553 |

Table S3: Structural details of Nb$M$Te$_4$ (M= Ir, Rh). Fractional atomic coordinates $(x, y, z)$ of LDA-optimized structures, with the lattice constants: $a = 3.77$ Å, $b = 12.51$ Å, $c = 13.12$ Å for NbIrTe$_4$, and $a = 3.757$ Å, $b = 12.638$ Å, $c = 13.102$ Å for NbRhTe$_4$.

| | | NbIrTe$_4$ | | | NbRhTe$_4$ | | |
|---|---|---|---|---|---|---|---|
| **No.** | **Atom** | $x$ | $y$ | $z$ | $x$ | $y$ | $z$ |
| 1 | Nb | 0 | 0.0544 | 0.0041 | 0 | 0.0536 | -0.1920 |
| 2 | Nb | 0 | 0.2719 | 0.4900 | 0 | 0.2717 | 0.2948 |
| 3 | Ir/Rh | 0 | 0.5650 | 0.9985 | 0 | 0.5339 | 0.8028 |
| 4 | Ir/Rh | 0 | 0.7561 | 0.4903 | 0 | 0.7550 | 0.2948 |
| 5 | Te | 0 | 0.0676 | 0.3903 | 0 | 0.0688 | 0.1955 |
| 6 | Te | 0 | 0.1924 | 0.8499 | 0 | 0.1917 | 0.6550 |
| 7 | Te | 0 | 0.3445 | 0.0951 | 0 | 0.3454 | 0.8980 |
| 8 | Te | 0 | 0.4157 | 0.6390 | 0 | 0.4149 | 0.4429 |
| 9 | Te | 0 | 0.5655 | 0.3929 | 0 | 0.5668 | 0.1988 |
| 10 | Te | 0 | 0.6762 | 0.8438 | 0 | 0.6741 | 0.6489 |
| 11 | Te | 0 | 0.8494 | 0.1069 | 0 | 0.8499 | 0.9107 |
| 12 | Te | 0 | 0.8929 | 0.6500 | 0 | 0.8914 | 0.4533 |

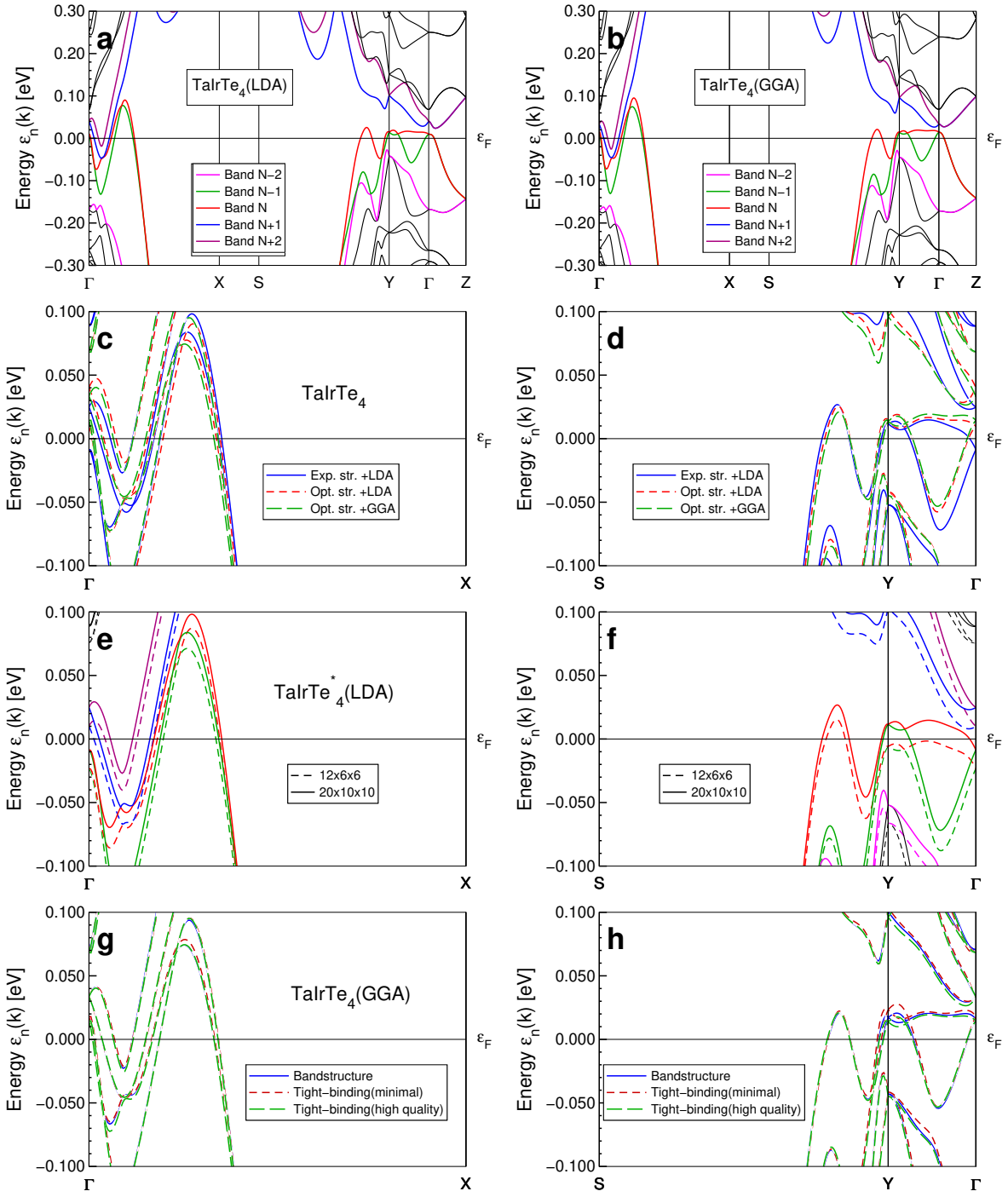


Figure S1: A detailed comparison of the electronic properties (bandstructures) of $TaIrTe_4$ between different crystal structures, $k$-mesh, and XC functional. Note that the optimized structures (Opt str.) correspond to LDA-optimized structures. Spin-orbit effects were included.

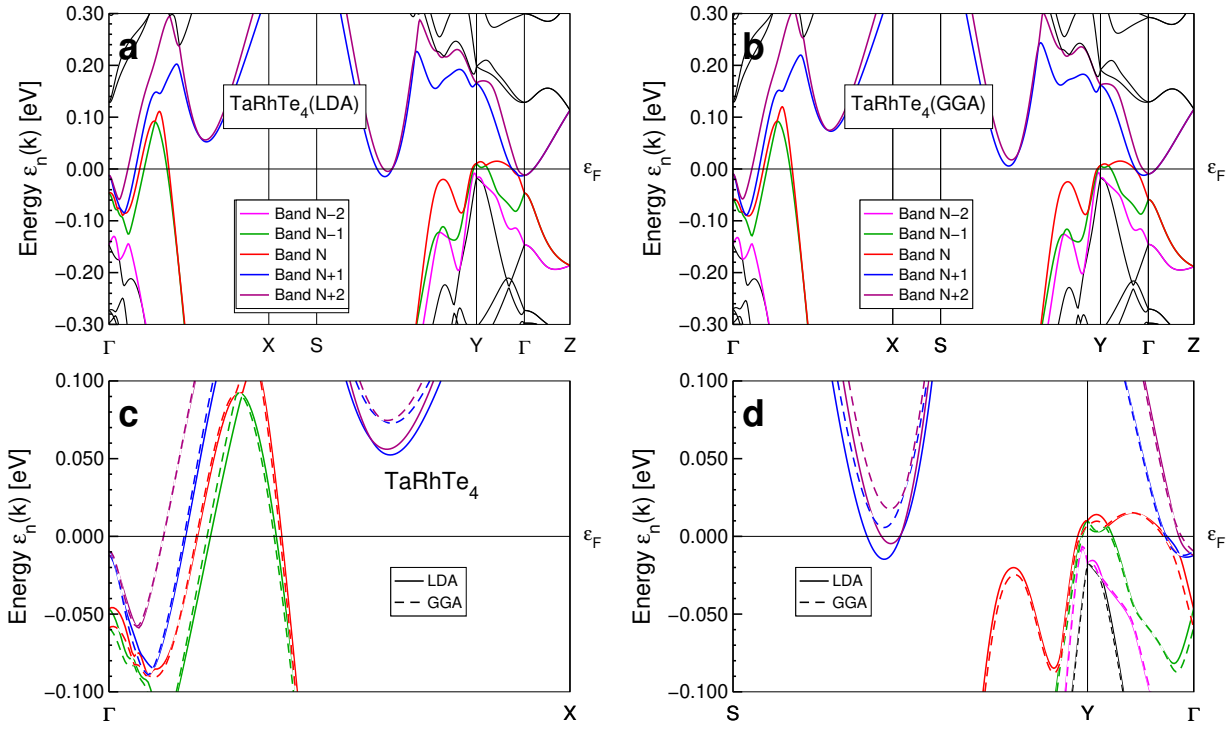


Figure S2: A detailed comparison of the electronic properties (bandstructure) of $TaRhTe_4$ between different $k$-mesh and XC functionals for the LDA-optimized structures of $TaRhTe_4$. Spin-orbit effects were included.

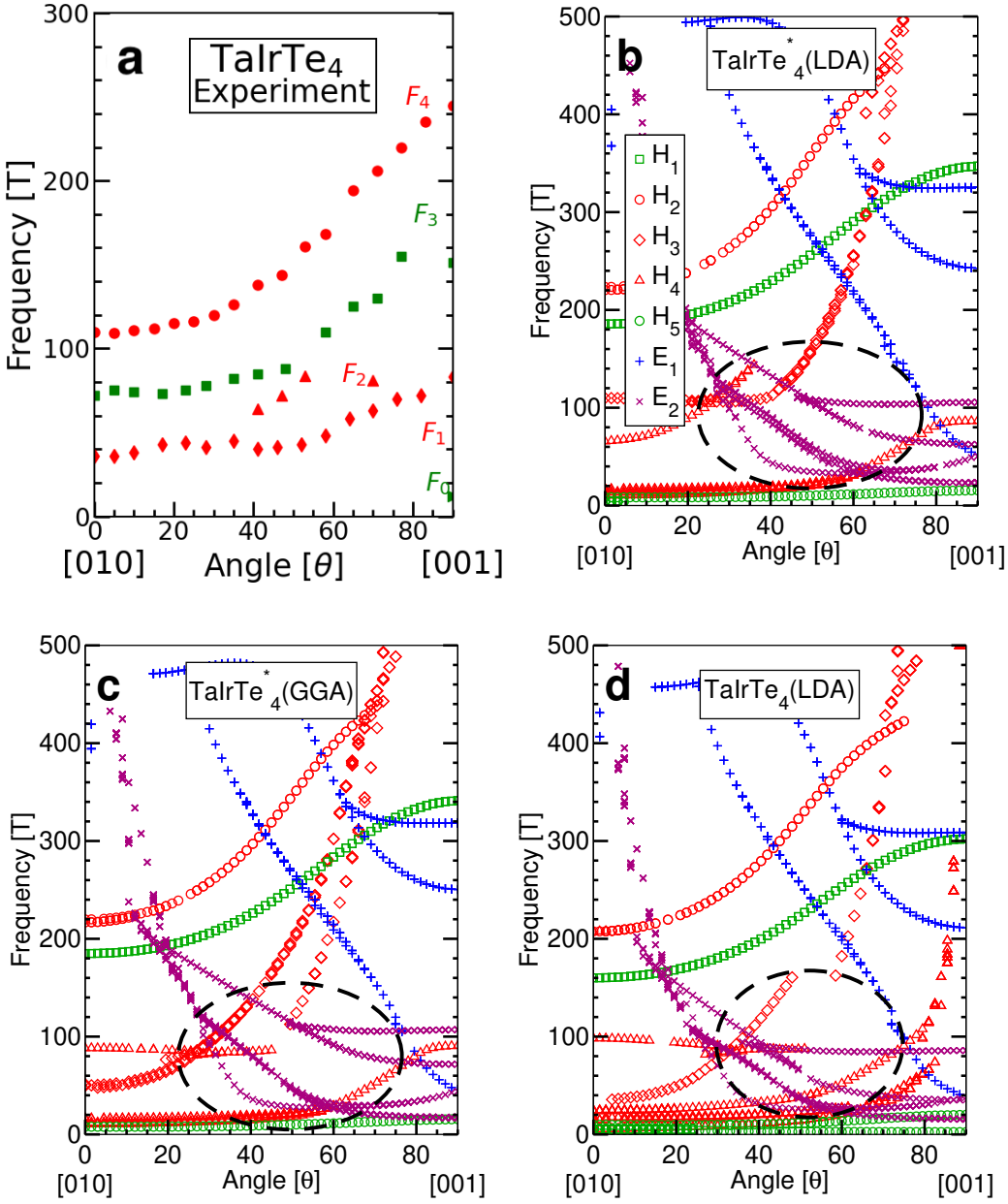


Figure S3: A detailed comparison of the dHvA frequencies between observed different crystal structures and XC functional. The experimental data is shown in (a). (b) and (c) correspond to the DFT calculations using the experimental crystal structure with a dense $k$-mesh, while (d) corresponds to DFT calculations on the LDA-optimized structure using LDA.

Table S4: Comparison of the Fermi velocity ($v_{\mathrm{F}}$), dHvA frequencies and their associated energy values for different magnetic field orientations, extracted from the observed dHvA data and DFT simulations. Observed frequencies (curves) are labeled $F_i$, while the electron and hole pockets are labeled $E_i$ and $H_i$, repectively.

| | **Curve** | **Fermi Velocity (m/s)** | | **Frequency (T)** | | **Energy (meV)** | |
|---|---|---|---|---|---|---|---|
| | | **B‖b** | **B‖c** | **B‖b** | **B‖c** | **B‖b** | **B‖c** |
| | F1 | $1.92*10^5$ | $2.87*10^5$ | 36 | 82 | 40.2 | 90.6 |
| **Experimental** | F2 | $1.04*10^5$ | | 36 | | 21.8 | |
| **Data** | F3 | $1.48*10^5$ | $2.12*10^5$ | 73.5 | 150 | 44.3 | 90.6 |
| | F4 | $1.80*10^5$ | $2.67*10^5$ | 109 | 245 | 65.5 | 144.3 |
| | H1 | $1.48*10^5$ | $2.12*10^5$ | 185 | 345 | 70.2 | 137.3 |
| **Exp. str.** | H2 | $1.80*10^5$ | $2.67*10^5$ | 210 | 460 | 91.0 | 199.7 |
| **(LDA)** | H3 | $1.04*10^5$ | | 110 | | 38 | |
| | H4 | $1.92*10^5$ | $2.87*10^5$ | 65 | 85 | 54.0 | 92.3 |
| | H1 | $1.48*10^5$ | $2.12*10^5$ | 185 | 340 | 70.2 | 136.3 |
| **Exp. str.** | H2 | $1.80*10^5$ | $2.67*10^5$ | 220 | 440 | 93.1 | 195.3 |
| **(GGA)** | H3 | $1.04*10^5$ | | 50 | | 25.6 | |
| | H4 | $1.92*10^5$ | $2.87*10^5$ | 90 | 90 | 63.5 | 95.0 |
| | H1 | $1.48*10^5$ | $2.12*10^5$ | 160 | 310 | 65.3 | 130.2 |
| **Opt. str.** | H2 | $1.80*10^5$ | $2.67*10^5$ | 210 | 430 | 91.0 | 193.1 |
| **(LDA)** | H3 | $1.04*10^5$ | | 40 | | 22.9 | |
| | H4 | $1.92*10^5$ | $2.87*10^5$ | 100 | 140 | 67.0 | 118.4 |
| | H1 | $1.48*10^5$ | $2.12*10^5$ | 160 | 300 | 65.3 | 128.1 |
| **Opt. str.** | H2 | $1.80*10^5$ | $2.67*10^5$ | 200 | 420 | 88.8 | 190.8 |
| **(GGA)** | H3 | $1.04*10^5$ | | 30 | | 19.9 | |
| | H4 | $1.92*10^5$ | $2.87*10^5$ | 75 | 120 | 58.0 | 109.6 |

Table S5: Calculated energy shifts, $\delta E = E_{\mathrm{Exp}} - E_{\mathrm{DFT}}$, between the observed dHvA frequencies ($F_i$) and the calculated frequencies from various fermion pockets ($H_i$ and $E_i$), required to match our DFT results with experimental values. Extracted parameters from Table S4 were used.

| **Curve** | **Energy Difference (meV)** | | | | | | | |
|---|---|---|---|---|---|---|---|---|
| | **Exp.-str. (LDA)** | | **Exp.-str. (GGA)** | | **Opt.-str. (LDA)** | | **Opt.-str. (GGA)** | |
| | **B‖b** | **B‖c** | **B‖b** | **B‖c** | **B‖b** | **B‖c** | **B‖b** | **B‖c** |
| F3-H1 | -26.0 | -46.8 | -26.0 | -45.8 | -21.0 | -39.6 | -21.0 | -37.5 |
| F4-H2 | -25.4 | -55.5 | -27.6 | -51.1 | -25.4 | -48.8 | -23.2 | -46.6 |
| F2-H3 | -16.3 | | -3.9 | | -1.2 | | 1.9 | |
| F1-H4 | -13.8 | -1.6 | -23.3 | -4.3 | -26.8 | -27.8 | -17.8 | -19.0 |

Table S6: WP landscape in $TaIrTe_4$. Band, Energy (E), BZ position, chirality ($\chi$) and type of WP in $TaIrTe_4$. Comparison is drawn between the results of LDA calculation for the experimental(Exp.-str.) and optimized structure (Opt.-str.) and GGA calculation for the optimized structure. The energies $E$ are in meV, the BZ positions are in the units of $2\pi/a$, and the degeneracy of the WPs is denoted by $d$. Spin orbit effects were included for all cases.

| | | | **Exp.-str. (LDA)** | | | | | **Opt.-str. (LDA)** | | | | | **Opt.-str. (GGA)** | | | | | |
|---|---|---|---|---|---|---|---|---|---|---|---|---|---|---|---|---|---|---|
| **Band** | **WP** | $\chi$ | $E$ | $k_x$ | $k_y$ | $k_z$ | $d$ | $E'$ | $k'_x$ | $k'_y$ | $k'_z$ | $d'$ | $E$" | $k_x$" | $k_y$" | $k_z$" | $d$" | **Type** |
| N | $W_1$ | -1 | 102.3 | 0.122 | 0.168 | 0.000 | 4 | 98.5 | 0.126 | 0.051 | 0.000 | 4 | 98.4 | 0.122 | 0.046 | 0.000 | 4 | I |
| N | $W_2$ | -1 | | | | | | | | | | | -44.1 | 0.054 | 0.008 | 0.000 | 4 | II |
| N | $W_3$ | 1 | | | | | | | | | | | -53.3 | 0.047 | 0.017 | 0.034 | 8 | II |
| N-1 | $P_1$ | -1 | 7.2 | 0.104 | 0.101 | 0.000 | 4 | 12.6 | 0.110 | 0.095 | 0.000 | 4 | 9.6 | 0.106 | 0.092 | 0.000 | 4 | II |
| N-1 | $P_2$ | 1 | -0.2 | 0.101 | 0.102 | 0.000 | 4 | -37.2 | 0.084 | 0.094 | 0.000 | 4 | -46.3 | 0.080 | 0.090 | 0.000 | 4 | II |
| N-1 | $P_3$ | 1 | -84.2 | 0.062 | 0.058 | 0.000 | 4 | -89.0 | 0.059 | 0.063 | 0.000 | 4 | -93.1 | 0.058 | 0.067 | 0.000 | 4 | |
| N-1 | $P_4$ | -1 | -104.1 | 0.055 | 0.058 | 0.063 | 8 | -87.4 | 0.029 | 0.056 | 0.059 | 8 | -82.4 | 0.027 | 0.052 | 0.055 | 8 | |
| N-1 | $P_5$ | 1 | -110.3 | 0.039 | 0.050 | 0.070 | 8 | -102.8 | 0.057 | 0.060 | 0.063 | 8 | -100.2 | 0.058 | 0.061 | 0.057 | 8 | |
| N-2 | $Q_1$ | 1 | -98.1 | 0.019 | 0.067 | 0.000 | 4 | -81.4 | 0.017 | 0.072 | 0.000 | 4 | -81.5 | 0.019 | 0.075 | 0.000 | 4 | |
| N-2 | $Q_2$ | 1 | -106.5 | 0.028 | 0.100 | 0.039 | 8 | -91.1 | 0.028 | 0.090 | 0.000 | 4 | -86.6 | 0.026 | 0.092 | 0.000 | 4 | |
| N-2 | $Q_3$ | -1 | -107.2 | 0.010 | 0.083 | 0.054 | 8 | -97.6 | 0.064 | 0.070 | 0.000 | 4 | -98.21 | 0.060 | 0.071 | 0.000 | 4 | |
| N-2 | $Q_4$ | -1 | -112.9 | 0.031 | 0.083 | 0.000 | 4 | -100.8 | 0.059 | 0.071 | 0.012 | 8 | -99.6 | 0.059 | 0.072 | 0.005 | 8 | |
| N-2 | $Q_5$ | -1 | -134.9 | 0.043 | 0.039 | 0.000 | 4 | -130.5 | 0.045 | 0.036 | 0.000 | 4 | -131.2 | 0.045 | 0.039 | 0.000 | 4 | |
| N-2 | $Q_6$ | -1 | -148.0 | 0.016 | 0.069 | 0.110 | 8 | -142.0 | 0.007 | 0.077 | 0.124 | 8 | | | | | | |

Table S7: WP landscape in $TaRhTe_4$. Band, Energy (E), BZ position, chirality ($\chi$) and type of WP in $TaRhTe_4$. Comparison is drawn between the results of LDA and GGA calculation for the optimized structure (Opt.-str.). The energies $E$ are in meV, the BZ position are in the units of $2\pi/a$, and degeneracy of the WPs is denoted by $d$. Spin-orbit effects were included for all cases.

| | | | **Opt-str. (LDA)** | | | | | **Opt-str. (GGA)** | | | | | |
|---|---|---|---|---|---|---|---|---|---|---|---|---|---|
| **Band** | **WP** | $\chi$ | $E$ | $k_x$ | $k_y$ | $k_z$ | $d$ | $E'$ | $k'_x$ | $k'_y$ | $k'_z$ | $d'$ | **Type** |
| N+1 | $V_1$ | -1 | 25.3 | 0.274 | 0.079 | 0.000 | 4 | 52.4 | 0.269 | 0.077 | 0.000 | 4 | |
| N+1 | $V_2$ | 1 | 14.3 | 0.043 | 0.064 | 0.000 | 4 | 14.7 | 0.040 | 0.067 | 0.000 | 4 | II |
| N+1 | $V_3$ | 1 | -17.5 | 0.010 | 0.020 | 0.000 | 4 | -24.8 | 0.013 | 0.022 | 0.000 | 4 | II |
| N | $W_1$ | -1 | 116.0 | 0.154 | 0.038 | 0.000 | 4 | 124.4 | 0.151 | 0.033 | 0.000 | 4 | I |
| N | $W_2$ | 1 | -44.2 | 0.017 | 0.016 | 0.000 | 4 | -43.1 | 0.020 | 0.033 | 0.000 | 4 | II |
| N | $W_3$ | 1 | -63.1 | 0.026 | 0.023 | 0.000 | 4 | -59.9 | 0.022 | 0.018 | 0.000 | 4 | II |
| N-1 | $P_1$ | -1 | -2.6 | 0.137 | 0.092 | 0.000 | 4 | -1.5 | 0.135 | 0.091 | 0.000 | 4 | II |
| N-1 | $P_2$ | 1 | -79.4 | 0.082 | 0.083 | 0.000 | 4 | -85.0 | 0.080 | 0.081 | 0.000 | 4 | II |
| N-1 | $P_3$ | 1 | | | | | | -91.4 | 0.032 | 0.029 | 0.026 | 8 | |
| N-1 | $P_4$ | -1 | | | | | | -114.3 | 0.035 | 0.035 | 0.048 | 8 | |
| N-1 | $P_5$ | -1 | -133.4 | 0.060 | 0.059 | 0.071 | 8 | -131.9 | 0.062 | 0.059 | 0.067 | 8 | |
| N-1 | $P_6$ | 1 | -137.7 | 0.046 | 0.046 | 0.072 | 8 | -133.1 | 0.041 | 0.041 | 0.064 | 8 | |
| N-2 | $Q_1$ | -1 | -12.5 | 0.005 | 0.145 | 0.023 | 8 | -11.0 | 0.005 | 0.147 | 0.021 | 8 | II |
| N-2 | $Q_2$ | 1 | -19.0 | 0.0136 | 0.136 | 0.000 | 4 | -15.7 | 0.012 | 0.140 | 0.000 | 4 | II |
| N-2 | $Q_3$ | 1 | -114.7 | 0.069 | 0.061 | 0.000 | 4 | -116.8 | 0.067 | 0.063 | 0.000 | 4 | |

Table S8: WP landscape in $NbIrTe_4$. Band, Energy (E), BZ position, chirality ($\chi$) and type of WP in $NbIrTe_4$. Comparison is drawn between the results of LDA and GGA calculation for the optimized structure (Opt.-str.). The energies $E$ are in meV, the BZ positions are in the units of $2\pi/a$, and the degeneracy of the WPs is denoted by $d$. Spin orbit effects were included for all cases.

| | | | **Opt-str. (LDA)** | | | | | **Opt-str. (GGA)** | | | | | |
|---|---|---|---|---|---|---|---|---|---|---|---|---|---|
| **Band** | **WP** | $\chi$ | $E$ | $k_x$ | $k_y$ | $k_z$ | $d$ | $E'$ | $k'_x$ | $k'_y$ | $k'_z$ | $d'$ | **Type** |
| N+1 | $V_1$ | -1 | 134.7 | 0.127 | 0.054 | 0.000 | 4 | 134.1 | 0.126 | 0.048 | 0.000 | 4 | |
| N+1 | $V_2$ | 1 | 96.1 | 0.112 | 0.050 | 0.000 | 4 | 92.2 | 0.111 | 0.042 | 0.000 | 4 | |
| N | $W_1$ | -1 | 127.3 | 0.147 | 0.055 | 0.000 | 4 | 131.7 | 0.145 | 0.052 | 0.000 | 4 | I |
| N | $W_2$ | -1 | 109.5 | 0.134 | 0.013 | 0.000 | 4 | 117.2 | 0.134 | 0.008 | 0.000 | 4 | II |
| N | $W_3$ | -1 | -58.8 | 0.072 | 0.009 | 0.000 | 4 | -56.9 | 0.071 | 0.006 | 0.000 | 4 | II |
| N | $W_4$ | 1 | -74.8 | 0.034 | 0.023 | 0.048 | 8 | -76.2 | 0.034 | 0.024 | 0.047 | 8 | III |
| N-1 | $P_1$ | 1 | -86.2 | 0.024 | 0.056 | 0.000 | 4 | -88.4 | 0.025 | 0.057 | 0.000 | 4 | |
| N-1 | $P_2$ | 1 | -95.8 | 0.200 | 0.052 | 0.000 | 4 | -87.1 | 0.201 | 0.040 | 0.000 | 4 | |
| N-2 | $Q_1$ | -1 | -69.2 | 0.013 | 0.141 | 0.036 | 8 | -71.2 | 0.014 | 0.140 | 0.036 | 8 | |
| N-2 | $Q_2$ | 1 | -101.3 | 0.028 | 0.106 | 0.000 | 4 | -102.1 | 0.027 | 0.107 | 0.000 | 4 | |
| N-2 | $Q_3$ | 1 | -115.5 | 0.065 | 0.044 | 0.000 | 4 | -116.9 | 0.066 | 0.044 | 0.000 | 4 | |
| N-2 | $Q_4$ | 1 | -139.4 | 0.042 | 0.075 | 0.057 | 8 | -137.9 | 0.042 | 0.070 | 0.051 | 8 | |

Table S9: WP landscape in $NbRhTe_4$. Band, Energy (E), BZ position, chirality ($\chi$) and type of WP in $NbRhTe_4$. Comparison is drawn between the results of LDA and GGA calculation for the optimized structure (Opt.-str.). The energies $E$ are in meV, the BZ positons are in the units of $2\pi/a$, and the degeneracy of the WPs is denoted by $d$. Spin orbit effects were included for all cases.

| | | | **Opt-str. (LDA)** | | | | | **Opt-str. (GGA)** | | | | | |
|---|---|---|---|---|---|---|---|---|---|---|---|---|---|
| **Band** | **WP** | $\chi$ | $E$ | $k_x$ | $k_y$ | $k_z$ | $d$ | $E'$ | $k'_x$ | $k'_y$ | $k'_z$ | $d'$ | **Type** |
| N+1 | $V_1$ | 1 | 81.6 | 0.038 | 0.080 | 0.000 | 4 | | | | | | |
| N+1 | $V_2$ | -1 | -21.7 | 0.026 | 0.035 | 0.000 | 4 | -33.1 | 0.021 | 0.030 | 0.000 | 4 | II |
| N | $W_1$ | -1 | 139.6 | 0.173 | 0.024 | 0.000 | 4 | 146.7 | 0.171 | 0.020 | 0.000 | 4 | III |
| N | $W_2$ | 1 | | | | | | -52.5 | 0.010 | 0.013 | 0.000 | 4 | II |
| N-1 | $P_1$ | -1 | -11.6 | 0.160 | 0.098 | 0.000 | 4 | -16.9 | 0.163 | 0.096 | 0.000 | 4 | II |
| N-1 | $P_2$ | 1 | -47.4 | 0.105 | 0.102 | 0.000 | 4 | -51.0 | 0.103 | 0.101 | 0.000 | 4 | II |
| N-1 | $P_3$ | -1 | | | | | | -148.9 | 0.005 | 0.006 | 0.058 | 8 | |
| N-2 | $Q_1$ | 1 | -69.3 | 0.020 | 0.135 | 0.000 | 4 | -72.1 | 0.020 | 0.136 | 0.000 | 4 | |
| N-2 | $Q_2$ | -1 | -111.5 | 0.025 | 0.007 | 0.000 | 4 | | | | | | |
| N-2 | $Q_3$ | 1 | -135.2 | 0.077 | 0.042 | 0.000 | 4 | -136.6 | 0.076 | 0.043 | 0.000 | 4 | |

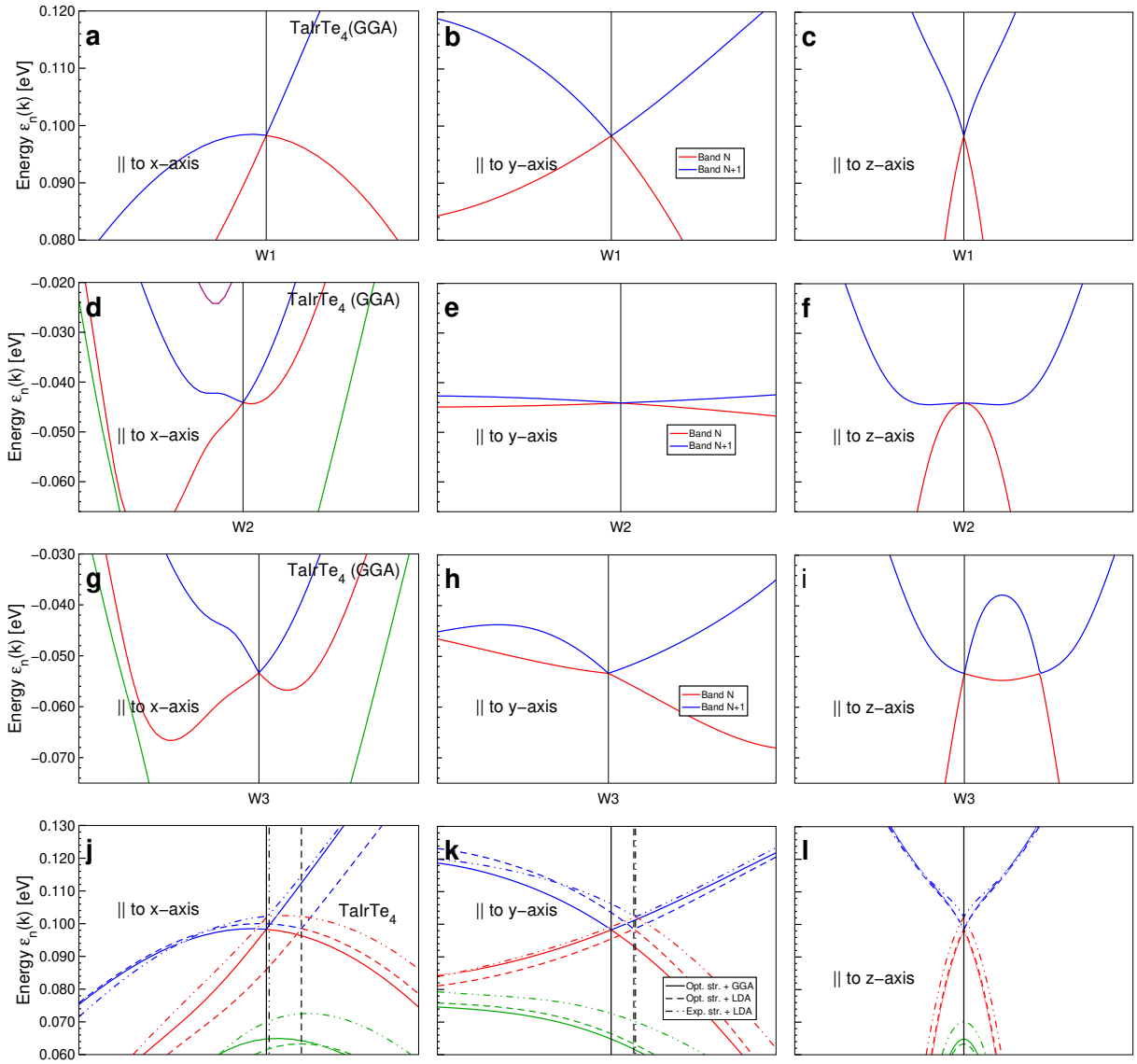


Figure S4: Low-energy dispersions along the three principal directions for the WPs from band (a-l) $N$ in $TaIrTe_4$, $W_1$ - $W_3$. All the three WPs are found to be of Type-II. The BZ positions of these WPs is listed in Table S6. Panels (j)-(l) show the comparison between the nature of WP $W_1$ between different structures, and XC functional, showing their evolution from type-II to type-I for the optimized structure.

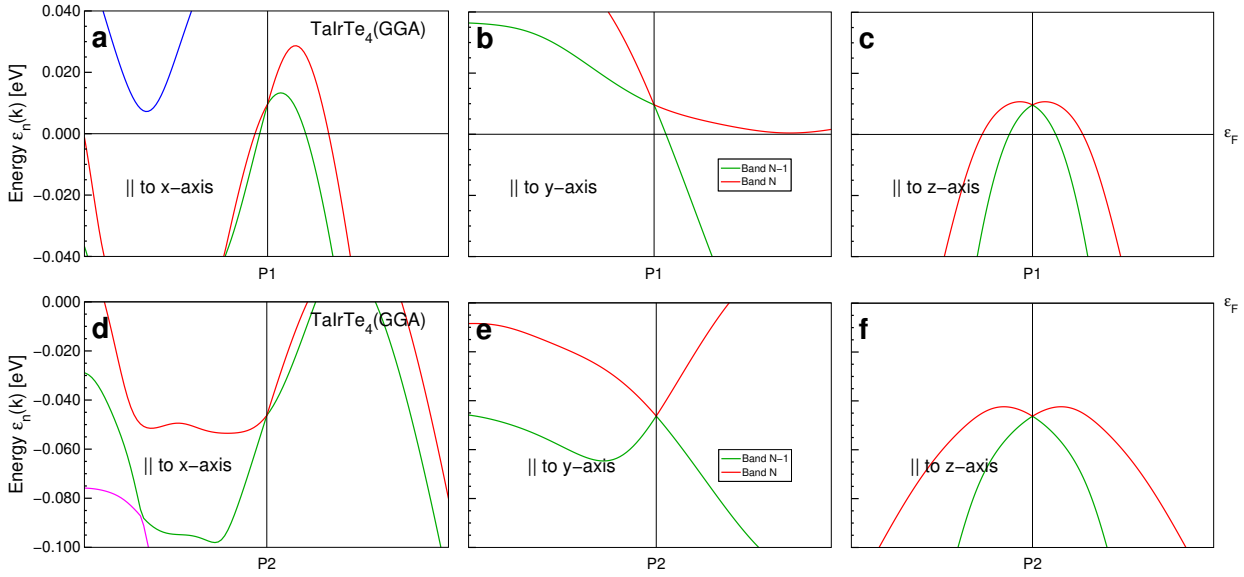


Figure S5: Low-energy dispersions along the three principal directions for the Fermi energy WPs from band (a-f) $N-1$ in $TaIrTe_4$, $P_1$ and $P_2$. Both the WPs are found to be of type-II. The BZ positions of these WPs is listed in Table S6.

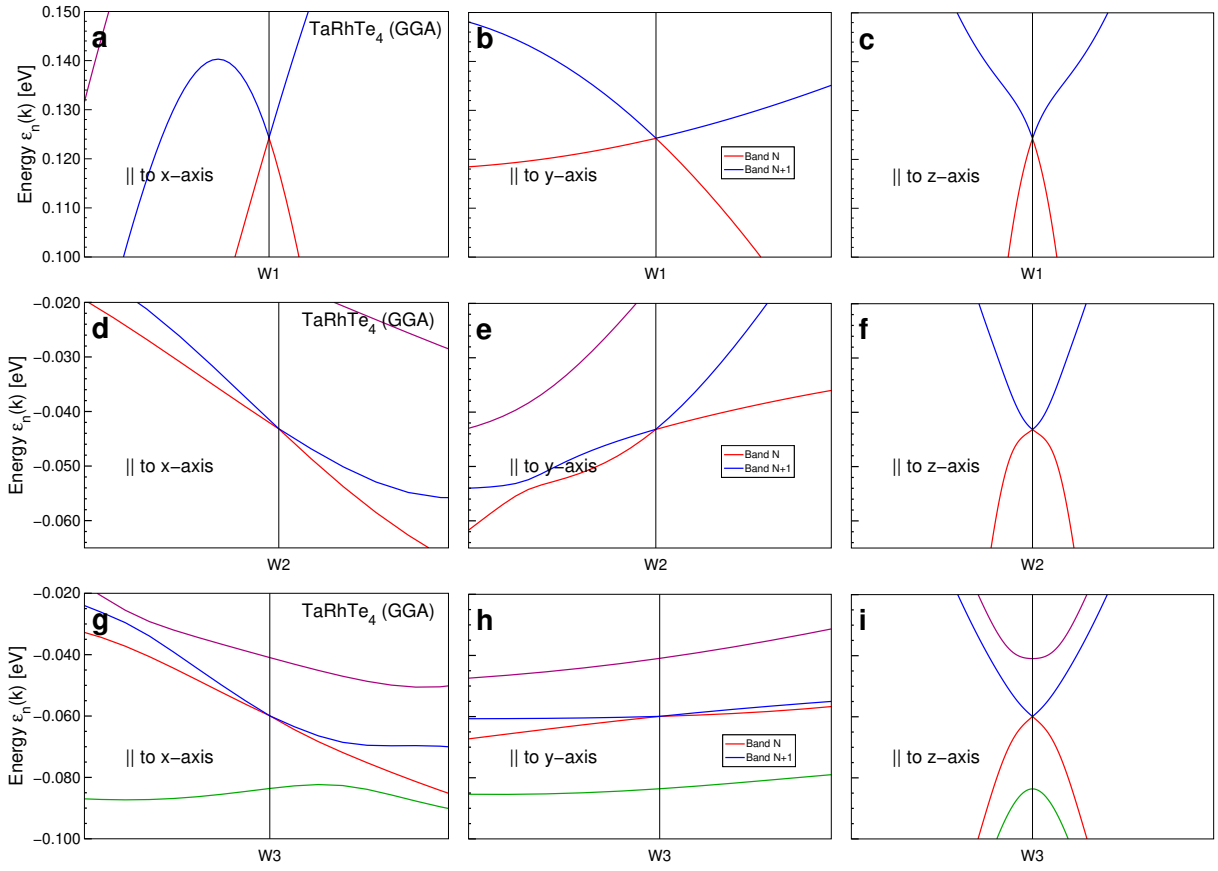


Figure S6: Low-energy dispersions along the three principal directions for the WPs from band (a-i) $N$ in $TaRhTe_4$, $W_1$ - $W_3$. $W_1$ is a type-I WP while $W_2$ and $W_3$ are of type-II. The BZ positions of these WPs is listed in Table S7.

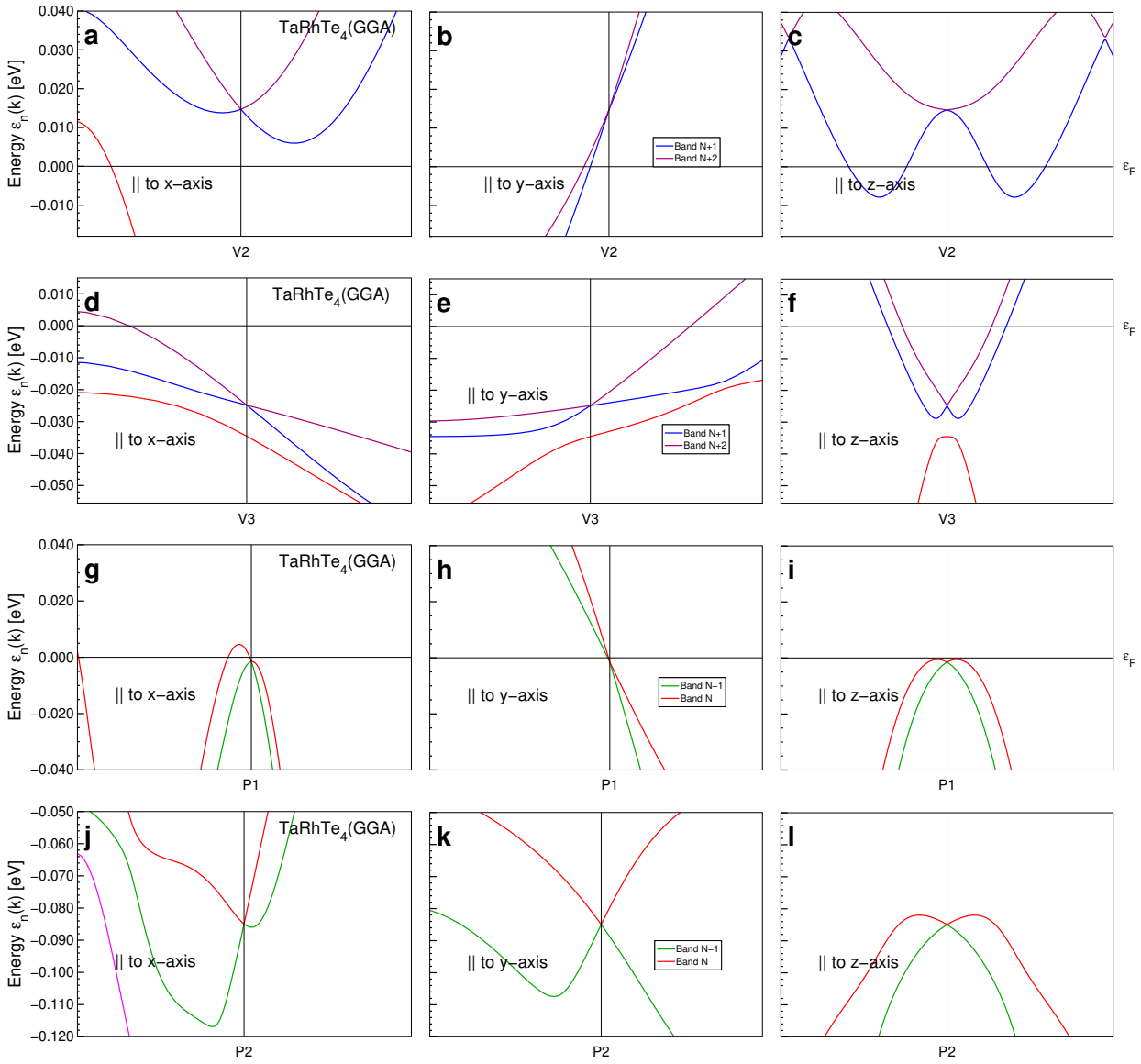


Figure S7: Low-energy dispersions along the three principal directions for the WPs from band (a-f) $N+1$ and (g-l) $N-1$ in $TaRhTe_4$, $V_2$, $V_3$, $P_1$ and $P_2$. All the four WP are of type-II. The BZ positions of these WPs is listed in Table S7.

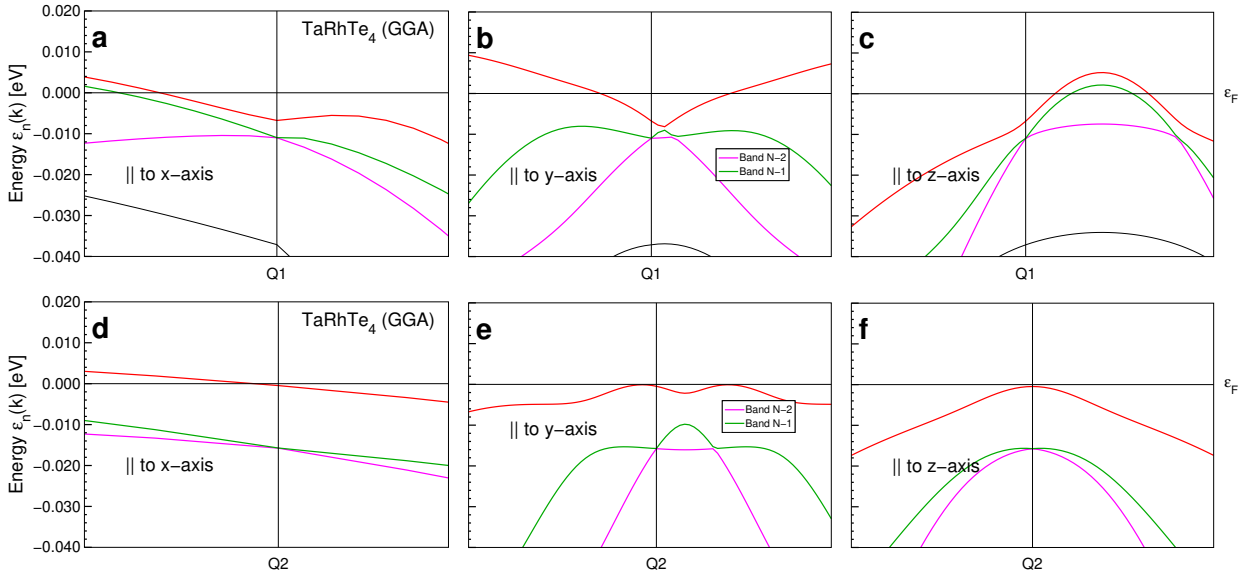


Figure S8: Low-energy dispersions along the three principal directions for the WPs from band (a-f) $N-2$ in $TaRhTe_4$, $Q_1$ and $Q_2$. Both WPs are of type-II. The BZ positions of these WPs is listed in Table S7.

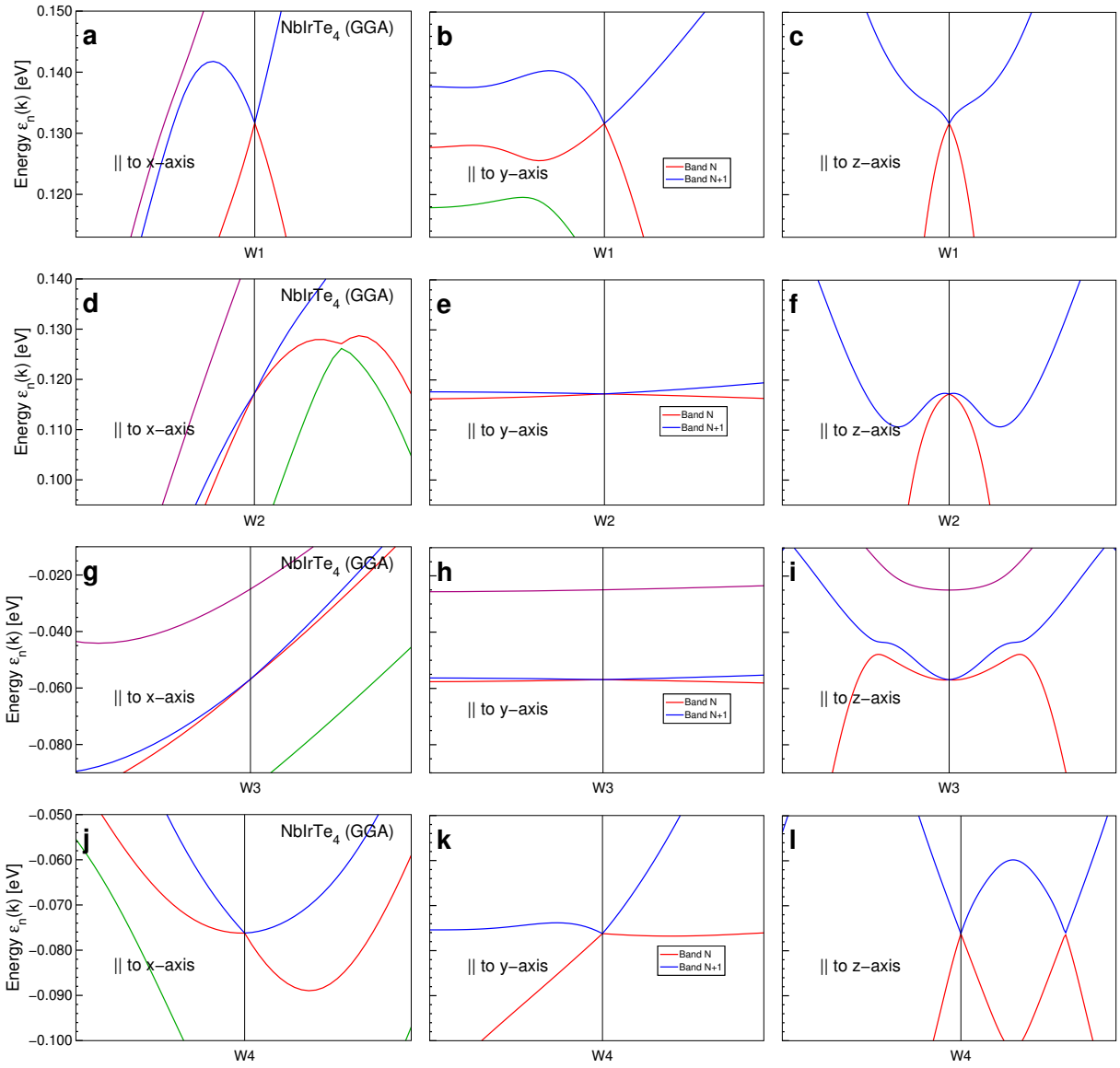


Figure S9: Low-energy dispersions along the three principal directions for the WPs from band (a-l) $N$ in $NbIrTe_4$, $W_1$ - $W_4$. $W_1$ is a type-I WP while $W_2$ and $W_3$ are of type-II and $W_4$ appears to be of type-III. The BZ positions of these WPs is listed in Table S8.

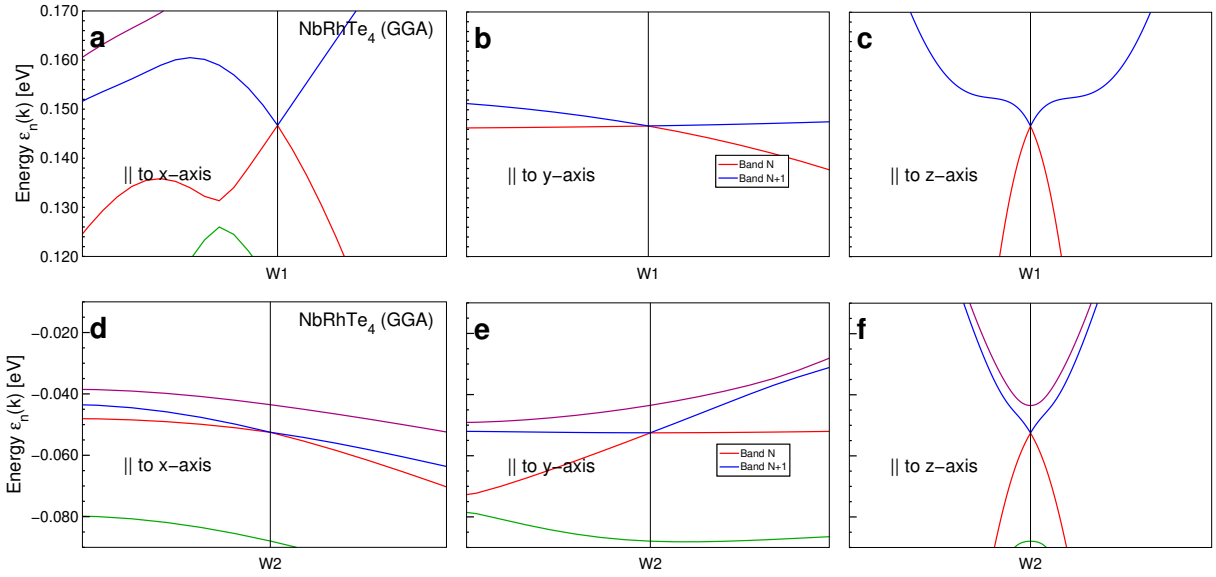


Figure S10: Low-energy dispersions along the three principal directions for the WPs from band (a-f) $N$ in $NbRhTe_4$, $W_1$ and $W_2$. $W_1$ is a type-I WP while $W_2$ is of type-II. The BZ positions of these WPs is listed in Table S9.

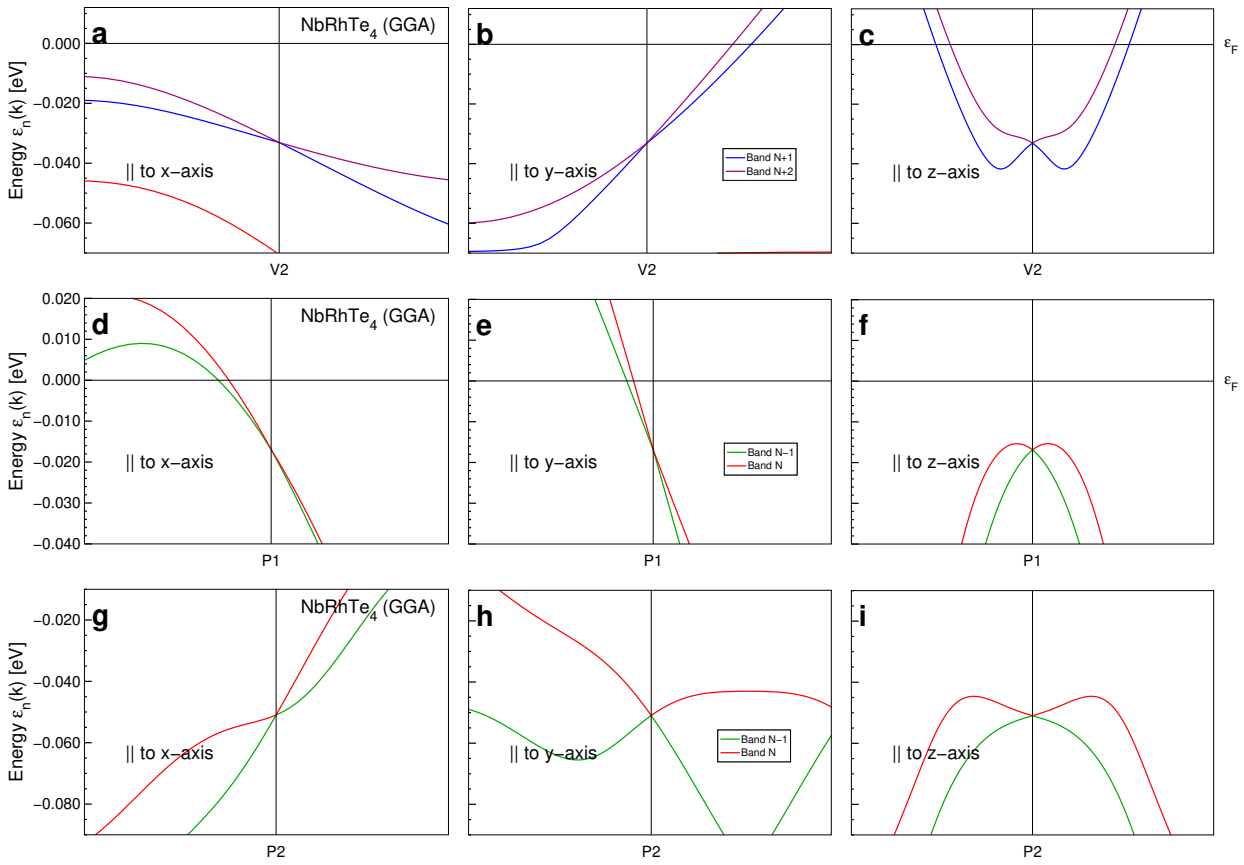


Figure S11: Low-energy dispersions along the three principal directions for the WPs from band (a-c) $N+1$ and (d-i) $N-1$ in $NbRhTe_4$, $V_2$, $P_1$ and $P_2$. All the three WPs are of type-II. The BZ positions of these WPs is listed in Table S9.

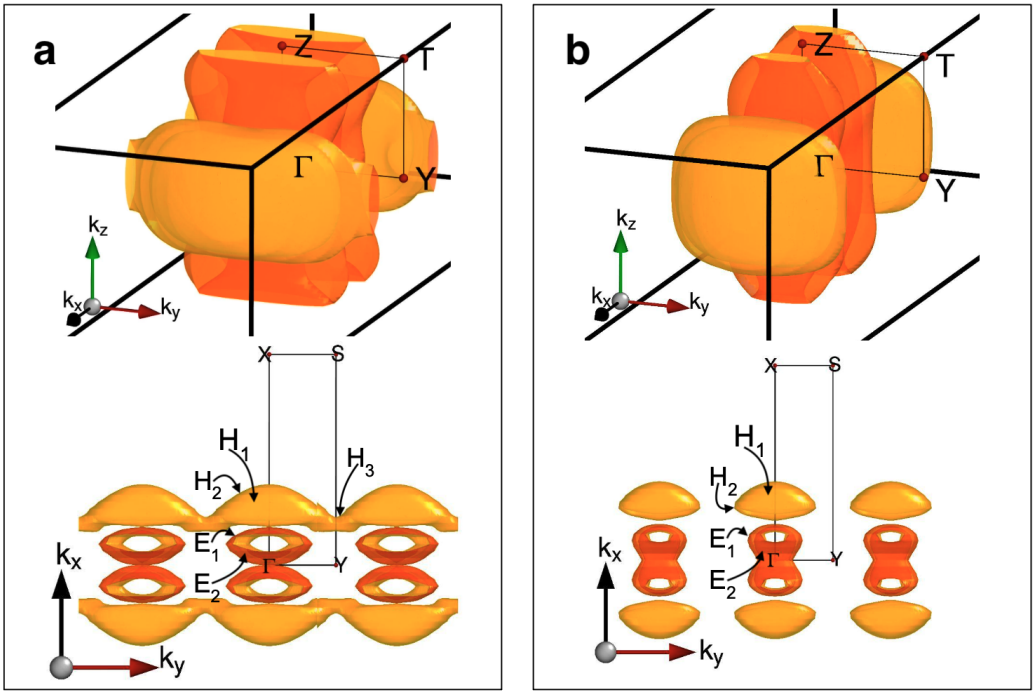


Figure S12: Calculated Fermi surface of Nb$M$Te$_4$ ($M$=Ir, Rh) within GGA, (a) NbIrTe$_4$ and (b) NbRhTe$_4$. We used a $k$-mesh with $120 \times 60 \times 60$ intervals to calculate the FS.

1. Koepernik, K. *et al.* $TaIrTe_4$: A ternary type-II Weyl semimetal. *Phys. Rev. B* **93**, 201101 (2016). URL https://link.aps.org/doi/10.1103/PhysRevB.93.201101.

2. Lee, J.-E. *et al.* Spin-orbit-splitting-driven nonlinear Hall effect in $NbIrTe_4$. *Nature Communications* **15** (2024). URL http://dx.doi.org/10.1038/s41467-024-47643-4.

3. Perdew, J. P. & Wang, Y. Accurate and simple analytic representation of the electron-gas correlation energy. *Phys. Rev. B* **45**, 13244–13249 (1992). URL https://link.aps.org/doi/10.1103/PhysRevB.45.13244.

4. Perdew, J. P., Burke, K. & Ernzerhof, M. Generalized gradient approximation made simple. *Physical Review Letters* **77**, 3865–3868 (1996). URL http://dx.doi.org/10.1103/PhysRevLett.77.3865.

5. Shipunov, G. *et al.* Layered van der Waals topological metals of $Ta{TM}Te_4$ ($TM$ = Ir, Rh, Ru) Family. *The Journal of Physical Chemistry Letters* **12**, 6730–6735 (2021). URL http://dx.doi.org/10.1021/acs.jpclett.1c01648.

6. Khim, S. *et al.* Magnetotransport and de Haas–van Alphen measurements in the type-II Weyl semimetal $TaIrTe_4$. *Phys. Rev. B* **94**, 165145 (2016). URL https://link.aps.org/doi/10.1103/PhysRevB.94.165145.

7. Onsager, L. Interpretation of the de Haas-van Alphen effect. *The London, Edinburgh, and Dublin Philosophical Magazine and Journal of Science* **43**, 1006–1008 (1952). URL http://dx.doi.org/10.1080/14786440908521019.